# Adaptively Compressed Exchange Operator for Large-Scale Hybrid Density Functional Calculations with Applications to the Adsorption of Water on Silicene

Wei Hu,*,[†] Lin Lin,*,‡,[†] Amartya S. Banerjee,*,[†] Eugene Vecharynski,*,[†] and Chao Yang*,[†]

[†]Computational Research Division, Lawrence Berkeley National Laboratory, Berkeley, California 94720, United States

[‡]Department of Mathematics, University of California, Berkeley, California 94720, United States

ABSTRACT: Density functional theory (DFT) calculations using hybrid exchange–correlation functionals have been shown to provide an accurate description of the electronic structures of nanosystems. However, such calculations are often limited to small system sizes due to the high computational cost associated with the construction and application of the Hartree–Fock (HF) exchange operator. In this paper, we demonstrate that the recently developed adaptively compressed exchange (ACE) operator formulation [*J. Chem. Theory Comput.* **2016**, *12*, 2242−2249] can enable hybrid functional DFT calculations for nanosystems with thousands of atoms. The cost of constructing the ACE operator is the same as that of applying the exchange operator to the occupied orbitals once, while the cost of applying the Hamiltonian operator with a hybrid functional (after construction of the ACE operator) is only marginally higher than that associated with applying a Hamiltonian constructed from local and semilocal exchange–correlation functionals. Therefore, this new development significantly lowers the computational barrier for using hybrid functionals in large-scale DFT calculations. We demonstrate that a parallel planewave implementation of this method can be used to compute the ground-state electronic structure of a 1000-atom bulk silicon system in less than 30 wall clock minutes and that this method scales beyond 8000 computational cores for a bulk silicon system containing about 4000 atoms. The efficiency of the present methodology in treating large systems enables us to investigate adsorption properties of water molecules on Ag-supported two-dimensional silicene. Our computational results show that water monomer, dimer, and trimer configurations exhibit distinct adsorption behaviors on silicene. In particular, the presence of additional water molecules in the dimer and trimer configurations induces a transition from physisorption to chemisorption, followed by dissociation on Ag-supported silicene. This is caused by the enhanced effect of hydrogen bonds on charge transfer and proton transfer processes. Such a hydrogen bond autocatalytic effect is expected to have broad applications for silicene as an efficient surface catalyst for oxygen reduction reactions and water dissociation.
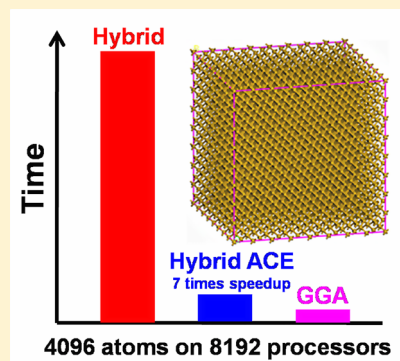
1. INTRODUCTION

Water adsorption on the surface of nanomaterials plays a crucial role in the fields in chemistry, biology, and materials science.[1] In particular, the interaction of water with noble metals and metal oxides has drawn considerable interest owing to the observation that these metals and metal oxides can serve as surface catalysts for partial water dissociation.[2−7] Therefore, they may be good candidate materials for molecular sensor and other photocatalytic solar energy applications. Compared to conventional three-dimensional (3D) metals and metal oxides,[1] two-dimensional (2D) materials[8−10] have larger reactive contact area for molecular adsorption. Therefore, they are expected to be more effective surface catalysts for molecular chemisorption and dissociation. However, it has been found that the adsorption energies of water molecules on most 2D materials such as graphene,[11−13] germanene,[14−16] phosphorene,[17−19] and molybdenum disulfide (MoS_2),[20−22] are rather small due to weak van der Waals interactions of water molecules physisorption on these 2D materials. The weak adsorption property prevents these materials from being used

directly as practical molecular sensors or efficient catalysts for oxygen reduction reaction and water dissociation without introducing dopants or defects.[23,24]

In this paper, we examine the possibility of using silicene as a surface catalyst for water dissociation through computation. Silicene is a 2D silicon monolayer similar to graphene but with buckled honeycomb structures.[25−28] Although it shares many similar properties with graphene, silicene exhibits a much higher chemical reactivity for atomic and molecular adsorption than graphene due to its buckled honeycomb structures.[29−32] In order to determine theoretically whether silicene is a promising metal-free 2D catalyst for water chemisorption and dissociation, we need to obtain an accurate description of the electronic structures of molecules and silicene-based nanosystems. These electronic structure properties include the energy position of the highest occupied and lowest unoccupied molecular orbitals (HOMO/LUMO) of molecules, the valence

band maximum (VBM) and conduction band minimum (CBM) of semiconductors and the work functions (the energy difference between the vacuum level and the Fermi level) of metals. These electronic properties can help elucidate the interfacial chemical reactions of molecular adsorption on the catalyst surfaces.[33−35] We use Kohn−Sham density functional theory (KSDFT)-based[36,37] computational methods to calculate the desired electronic properties of water molecules and a silicene-based substrate. The accuracy of this type of calculation depends strongly on the choice of the exchange and correlation functionals. The widely used semilocal LDA-PZ[38] and GGA-PBE[39] functionals often fail to give accurate electronic structures in such systems due to the lack of long-range nonlocal Hartree−Fock exchange interaction in the KSDFT calculations.

Hybrid density functionals, such as B3LYP,[40] PBE0,[41] and HSE,[42] have already been shown to improve the accuracy of KSDFT calculations by incorporating a fraction of the Hartree−Fock exact exchange or screened exchange operator into the Kohn−Sham Hamiltonian. In particular, DFT calculations with HSE functionals have been widely used to predict accurate adsorption energies for stable adsorption sites and electronic structures for molecular frontier level alignment relative to metals and semiconductors, for molecular adsorption on surfaces.[33−35] However, hybrid-functional-based DFT calculations are considerably more costly than DFT calculations that make use of a local or semilocal exchange−correlation functional. When the KSDFT equations are expanded in a planewave basis, the cost of applying the (discretized) Hartree−Fock exact exchange operator to all occupied orbitals scales cubically with respect to the system size, but the preconstant of the computation is very large. Various numerical methods have been developed to reduce the computational cost of Hartree−Fock-like calculations, such as linear scaling methods.[43,44] However, these methods are only effective for large systems with a substantial band gap.[45−47]

The recently developed adaptively compressed exchange (ACE) operator technique[48] is an accurate and efficient method for accelerating hybrid functional calculations. The efficiency of ACE results from the reduced computational cost associated with the construction and application of the Hartree−Fock exchange operator without loss of accuracy. The ACE operator is a low-rank approximation to the exact or screened Hartree−Fock exchange operator. It produces the same effect as the exact or screened exchange operator when applied to the set of occupied orbitals. Because the construction of the ACE operator does not depend on the system's energy gap, the technique can be applied to metals, semiconductors, and insulators.

The advantage of using the ACE formulation in a sequential hybrid functional DFT calculation has been demonstrated in a previous publication.[48] In this paper, we systematically demonstrate that the ACE formulation is also suitable for a massively parallel hybrid functional DFT calculation and that it allows hybrid functional DFT calculations to be carried out for systems with a few thousands of atoms. Thus, it significantly lowers the computational barrier and enables the wider use of hybrid functional calculations in studying a variety of nanosystems.[46,49,50] We show that when the ACE technique is used for large-scale nanosystems, the computational cost of hybrid functional calculations is no longer completely dominated by the construction and application of the Fock exchange operator. The optimization of other components of

the computation, such as a proper choice of an eigensolver, become important. We will discuss the use of an eigensolver based on the Projected Preconditioned Conjugate Gradient (PPCG)[51] algorithm which outperforms the well-known LOBPCG (Locally Optimal Block Preconditioned Conjugate Gradient) algorithm[52] in the context of hybrid functional calculations.

With the help of ACE-enabled parallel hybrid functional DFT calculations, we are able to examine the adsorption and electronic properties of water molecules on silicene. We observe that water monomer, dimer, and trimer show contrasting adsorption behaviors on silicene. The additional water molecules in dimer and trimer configurations induce a transition from physisorption to chemisorption and then to dissociation, on silicene. We compare the computational results obtained from a GGA-PBE functional calculation and those obtained from the hybrid HSE06 functional calculations, and we find that the GGA-PBE calculations significantly underestimate the energy gaps of water molecules compared to what is observed in the hybrid HSE06 calculation. We also find that the work functions of metallic Ag-supported silicene depend less sensitively on the choice of exchange−correlation functionals. Therefore, hybrid density functional calculations can significantly improve the fidelity of electronic structure calculations for molecular frontier level alignment of adsorption of water molecules on the surfaces under investigation.

2. METHODOLOGY

2.1. ACE Formulation for Hybrid Density Functional Calculations. In this section, we briefly review the adaptively compressed exchange (ACE) operator formulation, in the context of hybrid functional calculations. The KSDFT equations in the pseudopotential approximation are defined as

$$H\psi_i = \left(-\frac{1}{2}\Delta + V_{PS} + V_H[\rho] + V_{XC}[\{\psi_i\}] \right)\psi_j = \varepsilon_i\psi_i \tag{1}$$

where $\{\varepsilon_i\}$ are the eigenvalues, $\{\psi_i\}$ are the orbitals and N_e is the number of electrons. The orbitals $\{\psi_i\}$ satisfy the orthogonal constraints as $\int \psi_i^*(\mathbf{r})\,\psi_j(\mathbf{r})\,d\mathbf{r} = \delta_{ij}$, and $\rho(\mathbf{r}) = \sum_{i=1}^{N_e} |\psi_i(\mathbf{r})|^2$ is the electron density. The second term V_{PS} is the pseudopotential operator, which is independent of the electron density. The third term $V_H[\rho]$ is the Hartree potential, which depends on the density $\rho(\mathbf{r})$ as

$$V_H[\rho](\mathbf{r}, \mathbf{r}') = \delta(\mathbf{r} - \mathbf{r}') \int \frac{\rho(\mathbf{r}')}{|\mathbf{r} - \mathbf{r}'|}d\mathbf{r}'$$

The fourth term is the exchange−correlation potential, which can be formally split as $V_{XC} = V_X + V_C$, where V_X models the exchange interaction, and V_C models the many body correlation effects. In LDA and GGA calculations, both the V_X and V_C terms only depend on the density.

However, hybrid density functionals mix a fraction of the exact exchange potential from Hartree−Fock (HF) theory or its screened version, with the exchange and correlation potentials from DFT functionals. For example, the HSE exchange−correlation functional[42] is widely used to accurately describe the electronic structures for molecules and semiconductors in computational chemistry and materials science,[33−35] and it uses an error function screened Coulomb potential to calculate the exchange portion of the energy. The HSE06 exchange−correlation energy[53] is

$$E_{XC}^{HSE}(\mu) = 0.25 E_X^{SR}(\mu) + 0.75 E_X^{PBE,SR}(\mu) + E_X^{PBE,LR} + E_C^{PBE} \tag{2}$$

where $E_X^{PBE,SR}$ and $E_X^{PBE,LR}$ refer to the short-range and long-range parts of the exchange contribution in the PBE functional,[39] respectively. E_X^{SR} is the short-range part of the Fock exchange energy, defined as

$$E_X^{SR}(\mu) = -\frac{1}{2} \sum_{i,j=1}^{N_e} \iint \psi_i(\mathbf{r})\psi_j(\mathbf{r})\psi_j(\mathbf{r}')\psi_i(\mathbf{r}') \frac{\mathrm{erfc}(\mu|\mathbf{r}-\mathbf{r}'|)}{|\mathbf{r}-\mathbf{r}'|} \mathrm{d}\mathbf{r}\mathrm{d}\mathbf{r}' \tag{3}$$

Here, erfc is the complementary error function, and μ is an adjustable parameter to control the screening length of the short-range part of the Fock exchange interaction.

When the parameter μ is fixed, the functional derivative of E_{XC}^{HSE} with respect to the Kohn−Sham orbitals gives the exchange correlation potential

$$V_{XC}^{HSE}(\mathbf{r}, \mathbf{r}') = 0.25 V_X^{HSE}(\mathbf{r}, \mathbf{r}') + V_{XC}^{PBE}(\mathbf{r})\delta(\mathbf{r} - \mathbf{r}') \tag{4}$$

Here V_{XC}^{PBE} is the exchange−correlation potential due to the contribution from the PBE functional and is a local potential, and V_X^{HSE} is a full rank, nonlocal operator, and depends on not only the density but also the occupied orbitals $\{\psi_j\}$ as

$$V_X^{HSE}[\{\psi_j\}](\mathbf{r}, \mathbf{r}') = -\sum_{j=1}^{N_e} \psi_j(\mathbf{r})\psi_j(\mathbf{r}')K(\mathbf{r}, \mathbf{r}') \tag{5}$$

Here $K(\mathbf{r}, \mathbf{r}') = \frac{\mathrm{erfc}(\mu|\mathbf{r}-\mathbf{r}'|)}{|\mathbf{r}-\mathbf{r}'|}$ is the screened Coulomb kernel.

When a large basis set such as the planewave basis set is used, the only viable operation is to apply V_X^{HSE} to e.g. occupied orbitals. This amounts to solving N_e^2 Poisson-like problems with FFT, and the computational cost is $O(N_g \log(N_g)N_e^2)$, where the N_g is the number of points in the FFT grid. This cost is asymptotically comparable to other matrix operations such as the QR factorization for orthogonalizing the Kohn−Sham orbitals which scales as $O(N_g N_e^2)$, but the $\log(N_g)$ prefactor is significantly larger. Therefore, the computation of the exchange term alone can take more than 95% of the computational time, and its cost overshadows the rest of the components in the Kohn−Sham solver.

Because the Fock exchange energy is only a small fraction (usually 5% or less) of the total energy, it is more efficient *not* to update the exchange operator in each self-consistent field iteration. For the conventional planewave-based electronic structure software packages, such as Quantum ESPRESSO,[54] the self-consistent field (SCF) iteration of all occupied orbitals can be separated into two sets of SCF iterations. In the inner SCF iteration, the orbitals defining the exchange operator V_X^{HSE} as in eq 5 are fixed, denoted by $\{\varphi_i\}$. Then the matrix-vector multiplication of V_X and an orbital ψ is given by

$$(V_X^{HSE}[\{\varphi_j\}]\psi)(\mathbf{r}) = -\sum_{j=1}^{N_e} \varphi_j(\mathbf{r})\int K(\mathbf{r}, \mathbf{r}')\varphi_j(\mathbf{r}')\psi(\mathbf{r}')\mathrm{d}\mathbf{r}' \tag{6}$$

With the exchange operator fixed, the Hamiltonian operator only depends on the electron density $\rho(\mathbf{r})$, which needs to be updated in each inner SCF iteration by solving the linear eigenvalue problem in eq 1. Once the inner SCF for the electron density is converged, the output orbitals can simply then be used as the input orbitals to update the exchange operator. The outer SCF iteration continues until convergence

is reached. The convergence of the outer iteration can be monitored by the convergence of, for example, the Fock exchange energy. Note that even with the exchange operators fixed by $\{\varphi_i\}$, N_e^2 Poisson-like equations still need to be solved in each matrix-vector multiplication $H\psi_i$ within each inner SCF iteration step.

The recently proposed adaptively compressed exchange (ACE) operator formulation[48] significantly reduces the cost of hybrid functional calculations, by means of solving N_e^2 Poisson-like equations only at the beginning of each *outer iteration*. This greatly reduces the computational cost of the HF exchange but without loss of accuracy. The ACE method constructs a low rank approximation of the exchange operator targeting only at N_e orbitals. The ACE formulation does not depend on the size of energy gaps in the systems and thus can be applied to metals, semiconductors, and insulators. Therefore, the ACE formulation is particularly suitable for large-scale hybrid density functional calculations in computational chemistry and materials science.

In the ACE formulation, in each outer iteration, for a given set of orbitals $\{\varphi_i\}_{i=1}^{N_e}$, we first compute

$$W_i(\mathbf{r}) = (V_X^{HSE}[\{\varphi\}]\varphi_i)(\mathbf{r}) \quad i = 1, ..., N_e \tag{7}$$

The adaptively compressed exchange operator, denoted by V_X^{ACE}, should satisfy the conditions

$$(V_X^{ACE}\varphi_i)(\mathbf{r}) = W_i(\mathbf{r}) \quad \text{and} \quad V_X^{ACE}(\mathbf{r}, \mathbf{r}') = V_X^{ACE}(\mathbf{r}', \mathbf{r}) \tag{8}$$

For simplicity, we assume real arithmetic is used, which is the case for molecules and solid state systems with Γ point sampling. The potential V_X^{ACE} is defined as

$$V_X^{ACE}(\mathbf{r}, \mathbf{r}') = \sum_{i,j=1}^{N_e} W_i(\mathbf{r})B_{ij}W_j(\mathbf{r}') \tag{9}$$

where $B = M^{-1}$ is a negative semidefinite matrix, and

$$M_{kl} = \int \varphi_k(\mathbf{r})W_l(\mathbf{r})\mathrm{d}\mathbf{r}$$

Perform Cholesky factorization for $-M$, that is, $M = -LL^T$, where L is a lower triangular matrix. Then we get $B = -L^{-T}L^{-1}$. We define the projection vector in the ACE formulation as

$$\xi_k(\mathbf{r}) = \sum_{i=1}^{N_e} W_i(\mathbf{r})(L^{-T})_{ik} \tag{10}$$

then the adaptively compressed exchange operator is given by

$$V_X^{ACE}(\mathbf{r}, \mathbf{r}') = -\sum_{k=1}^{N_e} \xi_k(\mathbf{r})\xi_k(\mathbf{r}') \tag{11}$$

We also remark that ACE can be readily used to reduce the computational cost of the exchange energy, without the need of solving any extra Poisson equation:

$$E_X^{HF} = \frac{1}{2} \sum_{i=1}^{N_e} \iint \psi_i(\mathbf{r})V_X^{ACE}(\mathbf{r}, \mathbf{r}')\psi_i(\mathbf{r}')\mathrm{d}\mathbf{r}\mathrm{d}\mathbf{r}'$$

$$= -\frac{1}{2} \sum_{i,k=1}^{N_e} \left(\int \psi_i(\mathbf{r})\xi_k(\mathbf{r})\mathrm{d}\mathbf{r}\right)^2 \tag{12}$$

The main advantage of the ACE formulation is the significantly reduced cost of applying V_X^{ACE} to a set of orbitals

than that of applying V_X. Once ACE is constructed, the cost of applying V_X^{ACE} to any orbital ψ is similar to the application of a nonlocal pseudopotential, thanks to its low rank structure. ACE only needs to be constructed once when φ_i's are updated in the outer iteration. After they are constructed, the ACE can be reused for all the subsequent inner SCF iterations for the electron density and each iterative step for solving the linear eigenvalue problem. Because each outer iteration could require 10−100 or more applications of the Hamiltonian matrix H, the cost associated with the solution of the Poisson problem is hence greatly reduced. The flowchart of iterative methods for solving Hartree−Fock-like equations in the ACE formulation will be given later in Figure 2.

The ACE technique is related to the projector-based compression of the exchange operator.[55−57] One difference between ACE and the projector-based compression is that the ACE compresses the exchange operator into a rank N_e operator if the exchange operator is to be applied to N_e orbitals, while the projector-based formulation constructs an operator that is of rank $3N_e$ and is hence slightly more expensive. The ACE formulation has also been recently adapted to compress other quantities in electronic structure calculations such as the polarizability operator.[58]

2.2. Choice of Iterative Methods for Solving Large-Scale Eigenvalue Problems. As discussed in the introduction, the computational cost of hybrid functional calculations is often dominated by the cost of matrix-vector multiplication $H\psi_i$ and, in particular, by the application of the exchange operator. The cost due to the choice of iterative eigensolver is often insignificant for small systems. In the ACE formulation, the cost of $H\psi_i$ in hybrid functional calculations is only marginally larger than that in LDA/GGA calculations. Therefore, other components of the algorithm, in particular the Rayleigh−Ritz step in iterative eigensolvers, can contribute significantly to the overall computational time for systems of large size.

For systems of relatively small sizes (up to hundreds of atoms), our default choice of the eigensolver is the LOBPCG algorithm.[52] The LOBPCG method solves the linear eigenvalue problem of the form $HX = X\Lambda$ by iteratively searching the minimum of the $\text{Tr}[X^T HX]$ with the orthogonality constraint $X^T X = I$ in a subspace spanned by $3N_e$ vectors $[X, W, P]$. More specifically

$$X \leftarrow XC_X + WC_W + PC_P \tag{13}$$

Here W is called a preconditioned residual

$$W = TR := T(HX - X(X^T HX)) \tag{14}$$

where $R = HX - X(X^T HX)$ is the residual, and T is a preconditioner. For planewave basis sets, we use the Teter preconditioner,[59] which can be efficiently implemented by Fourier transform. P represents a conjugate direction. The coefficients C_X, C_W, and C_P are obtained by computing the lowest N_e eigenpairs of the projected $3N_e \times 3N_e$ generalized eigenvalue problem

$$S^T HSC = S^T SC\Lambda \tag{15}$$

where $S = [X, W, P]$ is the trial subspace and $C = [C_X, C_W, C_P]^T$ are the optimal coefficients. The LOBPCG method is outlined in Algorithm 1.

Notice that when N_e is relatively small ($N_e \sim 10-1000$), the computational cost of the $3N_e \times 3N_e$ projected eigenvalue problem in the Rayleigh−Ritz step (i.e., step 5 of Algorithm 1) is negligible. However, when N_e is relative large ($N_e \sim 1000-$

Algorithm 1 LOBPCG method for solving the KSDFT eigenvalue problems $H\psi_i = \varepsilon_i \psi_i$.

Input: Hamiltonian matrix H and initial wavefunctions.
Output: Eigenvalues $\{\varepsilon_i\}_{i=1}^{N_e}$ and wave functions $\{\psi_i\}_{i=1}^{N_e}$.

1: Initialize X by $\{\psi_i^0\}_{i=1}^{N_e}$ and orthonormalize X.
2: **while** convergence not reached **do**
3:　Compute the preconditioned residual $W \leftarrow T(HX - X(X^T HX))$, where T is a preconditioner.
4:　Update the trial subspace $S \leftarrow [X, W, P]$.
5:　Solving the projected eigenvalue problem $S^T HSC = S^T SC\Lambda$ and obtain the coefficients $C = [C_X, C_W, C_P]^T$.
6:　Compute the conjugate gradient direction $P \leftarrow WC_W + PC_P$.
7:　Compute $X \leftarrow XC_X + P$.
8: **end while**
9: Update $\{\psi_i\}_{i=1}^{N_e} \leftarrow X$.

10000), the computational cost for solving such $3N_e \times 3N_e$ projected eigenvalue problem can become dominant and can no longer be ignored. Furthermore, because of the limited scalability of available kernels for solving dense eigenvalue problems, the Rayleigh−Ritz step also limits the parallel scalability of LOBPCG and becomes the bottleneck when using a thousand or more processors on modern high performance computing architectures.

The cost of the Rayleigh−Ritz step can be reduced by the recently developed PPCG algorithm.[51] The main idea of PPCG is to replace the $3N_e \times 3N_e$ projected eigenvalue problem by N_e subproblems, each of size 3×3. The computational cost of this step scales linearly with N_e and is negligibly small even when N_e is large. It should be noted that the Rayleigh−Ritz procedure in step 12 of Algorithm 2 is optional and, in practice, is performed periodically after every 5−10 iterations to transform the columns of X to eigenvector approximations. Furthermore, when PPCG is combined with the SCF procedure, the Rayleigh−Ritz problem (of size $N_e \times N_e$) has to be solved only once at the end of the SCF iteration. Therefore, the cost of PPCG can be significantly smaller than that of LOBPCG when N_e is large. The pseudocode of the PPCG algorithm is shown in Algorithm 2.

Algorithm 2 PPCG method for solving the KSDFT eigenvalue problems $H\psi_i = \varepsilon_i \psi_i$.

**Input:** Hamiltonian matrix H and initial wavefunctions.
Output: Eigenvalues $\{\varepsilon_i\}_{i=1}^{N_e}$ and wave functions $\{\psi_i\}_{i=1}^{N_e}$.

1: Initialize X by $\{\psi_i^0\}_{i=1}^{N_e}$ and orthonormalize X through the Cholesky factorization based QR decomposition (Cholesky QR).
2: **while** convergence not reached **do**
3:　Compute the preconditioned residual $W \leftarrow (I - XX^T)T((HX - X(X^T AX))$, where T is a preconditioner.
4:　**for** $j = 1, \cdots, N_e$ **do**
5:　　Set $S \leftarrow [x_j, w_j, p_j]$.
6:　　Compute the coefficients $c = [\alpha_j, \gamma_j, \gamma_j]^T$ of the eigenproblem $S^T HSc = \theta S^T Sc$ corresponding the smallest eigenvalue θ.
7:　　Compute $p_j \leftarrow \beta_j w_j + \gamma_j p_j$.
8:　　Compute $x_j \leftarrow \alpha_j x_j + p_j$.
9:　**end for**
10:　Update $X \leftarrow [x_1, \cdots, x_{N_e}]$ and $P \leftarrow [p_1, \cdots, p_{N_e}]$.
11:　Orthonormalize X using the Cholesky QR factorization.
12:　If needed, perform the Rayleigh-Ritz produce within span(X).
13: **end while**
14: Update $\{\psi_i\}_{i=1}^{N_e} \leftarrow X$.

2.3. Parallel Implementation. The ACE formulation is implemented in the DGDFT (Discontinuous Galerkin Density Functional Theory) software package.[60−62] DGDFT is a massively parallel electronic structure software package for large-scale DFT calculations of tens of thousands of atoms, which includes a self-contained module called PWDFT for performing conventional standard planewave-based electronic structure calculations, and we use the Message Passing Interface (MPI) to handle data communication. We adopt the Hartwigsen−Goedecker−Hutter (HGH) norm-conserving pseudopotentials.[63]

The collection of wave functions is denoted by $\Psi = [\psi_1, ..., \psi_{N_e}]$. We use two different types of data distribution partition for the wave functions in PWDFT, as shown in Figure

1. The column cyclic partition, as shown in Figure 1a, is used for applying the Hamiltonian operator to the wave functions Ψ
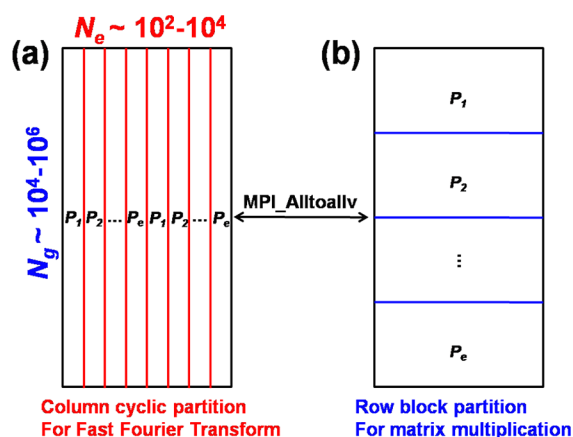
Figure 1. Two different types of partition of wave functions $\{\psi_i\}_{i=1}^{N_e}$ for the ACE formulation in PWDFT. The column cyclic partition as shown in (a) is used for Fast Fourier Transform (FFT) to compute exact exchange operator applied to wave functions $\{\psi_i\}_{i=1}^{N_e}$. The row block partition as shown in (b) is used when matrix−matrix multiplications are in the form $\varphi^T \psi$ and ψC.

without the ACE operator. For example, when applying the Laplacian operator to the orbitals using the Fast Fourier Transform (FFT), because each processor holds all entries of an orbital, the column partition allows the FFTs to be done in the same way as in a sequential implementation.

In order to apply the ACE operator, note that we do not explicitly store the ACE operator but only the projection vectors $\Xi = [\xi_1,...,\xi_{N_e}]$. The column size of Ξ is exactly the same as that of Ψ. The application of V_X^{ACE} to Ψ is similar to that of applying a set of nonlocal pseudopotentials. However, unlike the standard nonlocal pseudopotential vectors which are localized in the real space and could be stored as sparse vectors, the vectors Ξ are in general delocalized both in the real and in the Fourier space. Then the application of V_X^{ACE} can be performed as $V_X^{ACE}\Psi = -\Xi(\Xi^T\Psi)$. This involves two matrix−matrix multiplication operations: one in the form of $X^T Y$ and the other in the form of XC. Here the dimension of X and Y is $N_g \times N_e$, and the dimension of C is $N_e \times N_e$. In order to carry out the matrix products efficiently, we store Ξ as a dense matrix partitioned in row blocks as in Figure 1b, and we store $\Xi^T \Psi$ redundantly over all processors. In such a format, the operation in the form XC does not require any additional MPI communication, and the operation in the form X^TY only requires matrix products locally on each processor, followed by an MPI_Allreduce operation to sum up local products. We find that this format allows the parallel ACE implementation to scale to thousands of computational cores.

In order to perform such matrix−matrix multiplication, we need to transform Ψ from the column partition format to the row partition format. This conversion of the data distribution formats can be achieved using MPI_Alltoallv. Note that the row partition is also the natural format for performing matrix−matrix products in subsequent steps in an iterative linear eigensolver (LOBPCG or PPCG), the data conversion only needs to be done once per iteration step when solving the linear eigenvalue problem. In the eigensolvers, the Cholesky factorization and the Rayleigh−Ritz eigenvalue problems (The matrix dimensions are $3N_e$ and N_e respectively for LOBPCG

and PPCG algorithms) are performed in parallel using the ScaLAPACK[64] library.

At the beginning of a new outer SCF iteration, the ACE operator must be updated. This requires the solution of N_e^2 Poisson-like equations. The orbitals $\{\varphi_j\}$ are stored in the same column-wise cyclic distribution as of $\{\psi_j\}$ in Figure 1(a). For each MPI task, we broadcast the local $\{\varphi_j\}$ to other MPI processors by using the MPI_Bcast call, and then compute the integral $\int K (\mathbf{r},\mathbf{r}') \varphi_j(\mathbf{r}') \psi_i(\mathbf{r}') d\mathbf{r}'$ by solving the Poisson-like problem using FFT. This yields $\{W_i\}$ (eq 7), which is stored in the column-wise partition format. In order to construct the projection vectors $\{\xi_k\}$, the $\{W_i\}$ vectors are again transformed to the row partition to compute the matrix M as the inner product between W_i's and φ_j's. Cholesky factorization for the matrix $-M$ is performed, and finally $\{\xi_k\}$ are obtained by solving a triangular system using the Cholesky factors as in eq 10.

For conventional hybrid density functional calculations, the computation of the Fock exchange energy are expensive due to additional requirements of solving the Poisson equations for large systems even containing a few hundreds of atoms. However, in the framework of ACE formation, the computational cost of the Fock exchange energy defined in Equation 12 is greatly reduced, because we only require the matrix−matrix inner products in the column cyclic data distribution partition as shown in Figure 1b.

The flowchart of PWDFT for iterative methods to solve the KSDFT equations in the ACE formulation is shown in Figure 2, including two-level SCF structure. For large-scale hybrid density functional calculations in the ACE formulation, the main computational components are (a) solution of large-scale KSDFT eigenvalue problems and (b) construct the ACE operator. In particular, the application of the Hamiltonian operator in the ACE format is no longer expensive, and the cost is comparable to that of applying the Hamiltonian operator using local and semilocal exchange−correlation functionals.

3. RESULTS AND DISCUSSION

In this section, we first present some computational results that demonstrate the accuracy and efficiency of ACE-based hybrid functional DFT calculation for simple bulk silicon systems of various sizes. We then show that with such a powerful tool, we can carefully analyze the details of water molecules adsorption on Ag-supported two-dimensional silicene. The hybrid functional we use in the following calculation is the HSE06 functional.[53]

Figure 3 shows the geometric structures of several bulk silicon systems used in our computational experiments. We use eight bulk silicon systems to measure the scalability of the computation. These systems include Si_8 in a standard unit cell, Si_{64} in a $2 \times 2 \times 2$ supercell, Si_{216} in a $3 \times 3 \times 3$ supercell, Si_{512} in a $4 \times 4 \times 4$ supercell, Si_{1000} in a $5 \times 5 \times 5$ supercell, Si_{1728} in the $6 \times 6 \times 6$ supercell, Si_{2744} in the $7 \times 7 \times 7$ supercell and Si_{4096} in the $8 \times 8 \times 8$ supercell.

Table 1 lists the number N_{atom} of silicon atoms, the length $L_{supercell}$ (Å) of supercells, the number N_{band} of bands (or states), and the total number N_{grid} of grid points required to represent the ortbials in the real space for a given E_{cut}. All systems are closed shell with spin degeneracy excluded. Therefore, the number of bands is $N_{band} = N_e/2$. The total number of grid points N_{grid} is determined from the kinetic energy cutoff E_{cut} by the following rule:
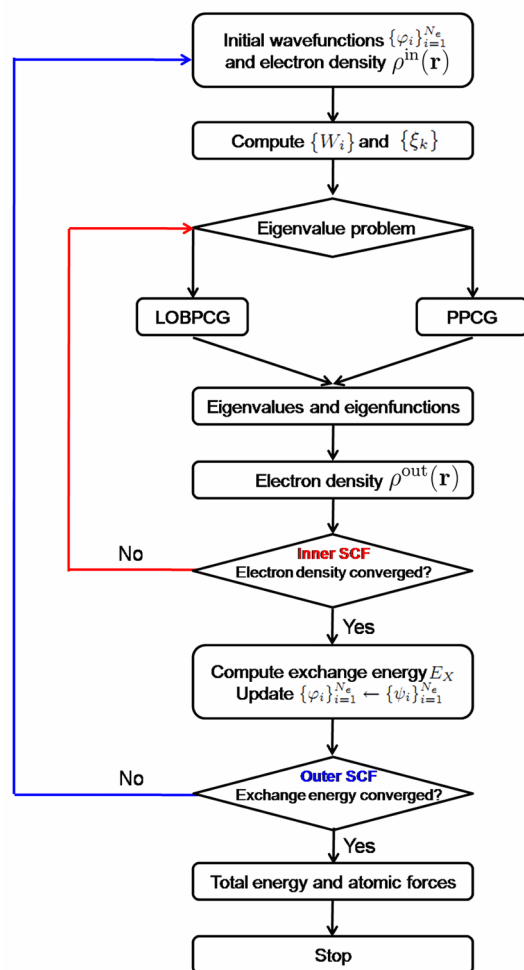
Figure 2. Flowchart of the ACE formulation for hybrid density functional calculations. The inner SCF iteration replaces the exchange operator V_X by the low rank operator V_X^{ACE}, and V_X^{ACE} is only updated at the beginning of each outer SCF iteration.
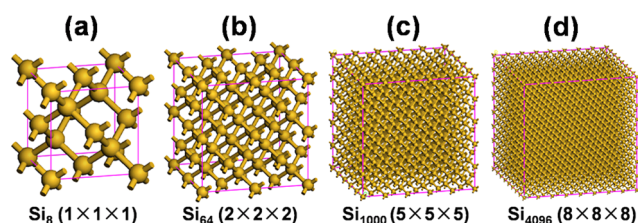
Figure 3. Geometric structures of bulk silicon systems used for the ACE formulation in PWDFT. (a) Si_8 in the unitcell, (b) Si_{64} in the $2 \times 2 \times 2$ supercell, (c) Si_{1000} in the $5 \times 5 \times 5$ supercell, and (d) Si_{4096} in the $8 \times 8 \times 8$ supercell.

$$(N_{grid})_i = \frac{\sqrt{2E_{cut}}\, L_i}{\pi} \qquad (16)$$

Here L_i is the length of supercells along the i-th coordinate direction. The total number of grid points is $N_{grid} = \prod_{i=1}^{3} (N_g)_i$. In a typical calculation $N_{grid} \sim 10^4 - 10^6$ and $N_{band} \sim 10^2 - 10^4$, as shown in Figure 1.

3.1. Accuracy. We first study the accuracy of the ACE calculation. Figure 4 shows how the errors in the computed HF energy ΔE_{HF} and energy band gap ΔE_{gap} of bulk silicon system Si_{64} change with respect to the E_{cut} parameter. We set a large

Table 1. Structural Properties of Bulk Silicon Systems Used for the ACE Formulation in PWDFT, Including the Number N_{atom} of Silicon Atoms, the length $L_{supercell}$ (Å) of Supercells, the Number N_{band} of Bands (or States), and the Total Number N_{grid} of Grid Points for Different Bulk Silicon Systems[a]

systems	N_{atom}	$L_{supercell}$ (Å)	N_{band}	N_{grid}
$Si_8(1 \times 1 \times 1)$	8	5.43	16	15^3
$Si_{64}(2 \times 2 \times 2)$	64	10.86	128	30^3
$Si_{216}(3 \times 3 \times 3)$	216	16.29	432	44^3
$Si_{512}(4 \times 4 \times 4)$	512	21.72	1024	60^3
$Si_{1000}(5 \times 5 \times 5)$	1000	27.15	2000	74^3
$Si_{1728}(6 \times 6 \times 6)$	1728	32.58	3456	88^3
$Si_{2744}(7 \times 7 \times 7)$	2744	38.01	5488	104^3
$Si_{4096}(8 \times 8 \times 8)$	4096	43.45	8192	118^3

[a]We set $E_{cut} = 10$ hartree to guarantee the accuracy of the calculations.
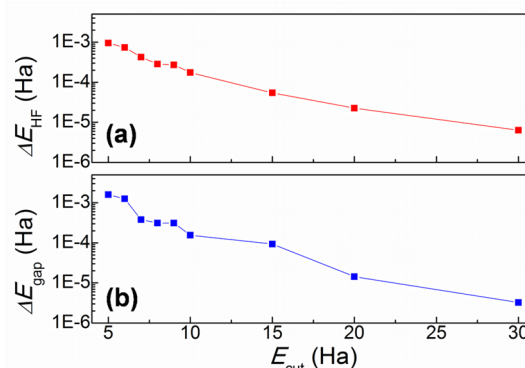
Figure 4. Computational accuracy of Si_{64} in terms of the HF energy error ΔE_{HF} (Hartree) and the energy gap error ΔE_{gap} (Hartree) with different kinetic energy cut off E_{cut} (Hartree).

$E_{cut} = 40$ hartree as the convergence reference results in the ACE calculations, and then we define the errors of the HF energy and energy band gap respectively as $\Delta E_{HF} = E_{HF} - E_{HF}(E_{cut} = 40 \text{ Ha})$ and $\Delta E_{gap} = E_{gap} - E_{gap}(E_{cut} = 40 \text{ Ha})$, where E_{HF} and E_{gap}, respectively, represent the HF energy and energy band gap, which are changed with respect to the energy cutoff E_{cut}. Our calculations show that the errors of the HF energy and energy gap can be as small as about 10^{-4} Hartree when the energy cutoff is set to 10 hartree. In the following hybrid density functional calculations of other bulk silicon systems about the convergence calculations and parallel performance, we set the energy cutoff E_{cut} to 10 hartree to guarantee the accuracy of the calculations.

We compare the computational results between the conventional hybrid DFT calculations and ACE-enabled hybrid DFT calculations in terms of the HF energy and the energy gap for the Si_{64}, Si_{216}, Si_{512}, and Si_{1000} systems, as shown in Table 2. Our calculations show that the ACE-enabled hybrid DFT calculations can give very accurate HF energy and energy gap (the energy difference is under 1×10^{-4} Hartree) even for large systems (Si_{1000}) compared to conventional hybrid DFT calculations. In fact, the ACE formulation is exact and does not introduce any error in hybrid functional calculations when the SCF convergence is reached. The small error of ACE formulation originates from our convergence criterion that the outer SCF iteration is terminated when the relative error of the

Table 2. Comparison Results between the Conventional Hybrid DFT Calculations and ACE-Enabled Hybrid DFT Calculations in Terms of the HF Energy E_{HF} (Hartree) and the Energy Gap E_{gap} (Hartree) for the Si_{64}, Si_{216}, Si_{512}, and Si_{1000} Systems[a]

methods	ACE HSE06 (LOBPCG)		conventional HSE06 (LOBPCG)	
systems	E_{HF}	E_{gap}	E_{HF}	E_{gap}
Si_{64}	-13.541616 (10^{-6})	1.488335	-13.541629	1.488352
Si_{216}	-45.471192 (10^{-7})	1.449790	-45.471190	1.449790
Si_{512}	-107.698011 (10^{-7})	1.324901	-107.698016	1.324902
Si_{1000}	-210.300628 (10^{-6})	1.289162	-210.300524	1.289128

[a]The corresponding relative errors of the HF energy are shown in the brackets.

exchange energy is smaller than 10^{-6}. When this criterion is tightened, the error can further decrease systematically.

3.2. Efficiency. We demonstrate the convergence of hybrid density functional calculations for the Si_{1000} system, which has 2000 occupied bands. Table 3 lists the number of inner

Table 3. Comparison between the Conventional Hybrid DFT Calculation and an ACE-Enabled Hybrid DFT Calculation in Terms of the Number of Inner SCF Iterations and Wall Clock Time Spent in Each outer SCF Iteration for Si_{1000} on 2000 Cores

methods	ACE HSE06 (LOBPCG)		conventional HSE06 (LOBPCG)	
no. outer SCF	no. inner SCF	time (s)	no. inner SCF	time (s)
1	6	356	6	2518
2	5	320	5	2044
3	5	308	4	1665

iterations taken in each of the first three outer SCF iterations. As expected, we can see that the use of ACE does not impact the number of inner SCF iterations per outer SCF iteration. Furthermore, the convergence property of hybrid DFT calculations with ACE in terms of the number of outer SCF iterations is comparable to that of the conventional algorithm.[48]

We also compare the wall clock time consumed by each outer SCF iteration with and without using the ACE formulation. The use of the ACE formulation significantly reduces the computational time. Note that in each outer SCF iteration that uses ACE, roughly 82 s are spent to update the low rank approximation to the exchange operator. For this ACE-enabled hybrid DFT calculation, each inner SCF iteration, which uses the LOBPCG eigensolver to compute 2000 or so eigenpairs, takes only 48 s compared to 365 s in conventional hybrid DFT calculation. We should also remark that we use the standard GGA functional (PBE)-based DFT calculation to generate the initial guesses of the orbitals required in the hybrid DFT calculation. For this problem, we ran 25 SCF iterations using the PBE GGA functional. This initial step takes 1286 s on 2000 cores.

Furthermore, we also study the comparison results of iterative methods for large-scale convergence hybrid density functional (HSE06) calculations by using the ACE formulation as shown in Figure 5. We find that the PPCG algorithm is about 2 times faster (22 s) than the LOBPCG algorithm (48 s) for the eigenvalue problems in each inner SCF iteration. The total wall time for these three methods (Conventional HSE06 (LOBPCG), ACE HSE06 (LOBPCG) and ACE HSE06 (PPCG)), respectively, is 9731, 2987, and 1322 s for hybrid density functional calculations on the Si_{1000} system (2000 bands) by using 2000 computational cores. Notice that these time includes the standard GGA-PBE calculations (1286 and
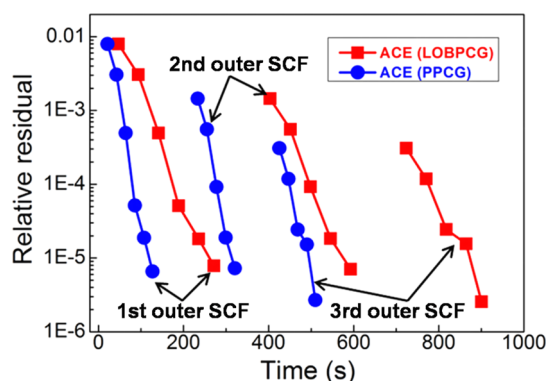
Figure 5. Comparison results of iterative methods for large-scale convergence hybrid density functional calculations (HSE06) by using the ACE formulation. Two different iterative algorithms (LOBPCG and PPCG) are used to solve KSDFT eigenvalue problems in the ACE formulation for hybrid density functional calculations on the Si_{1000} system (2000 bands) by using 2000 computational cores. We adopt the relative residual of total potential in the inner SCF iterations.

624 s, respectively, for LOBPCG and PPCG algorithms for 25 times inner SCF iterations) to initialize the oribitals for conventional hybrid functional (HSE06) calculations.

3.3. Parallel Scalability. Section 2.3 indicates that the construction and the application of the ACE operator can be efficiently parallelized. To illustrate the parallel scalability of the ACE approach in PWDFT, we examine how the wall clock time spent in each inner and outer SCF iteration changes with respect to both the number of cores (strong scaling) and the system size (weak scaling).

Figure 6a shows that the strong scalability of ACE is nearly perfect up to 2000 processors for the Si_{1000} systems, and Figure 6b shows the weak scalability of the ACE is nearly ideal for systems with up to 4096 atoms on 8192 cores. Figure 6c,d indicate that both the strong and weak scaling are mainly limited by the choice of eigensolver instead of the construction of the ACE operator, when more than 1000 processors are used.

Furthermore, we can see from Figure 6c that updating the ACE operator is the most expensive step in each outer SCF iteration even though its parallel scaling is nearly perfect. When the number of cores used in the computation is relatively small (a few hundred), it takes roughly 3−4 times more wall clock time to update the ACE operator than to complete inner SCF iterations (PPCG). We also observe that the cost of HF exchange energy computation is relatively low compared to the cost of updating the ACE operator. In the case of Si_{1000}, it only takes 0.4 s to compute the HF energy on 2000 computational cores, whereas 85 s are required to update the ACE operator.

To examine the parallel performance of the inner SCF iteration more closely, we examine the strong and weak scaling
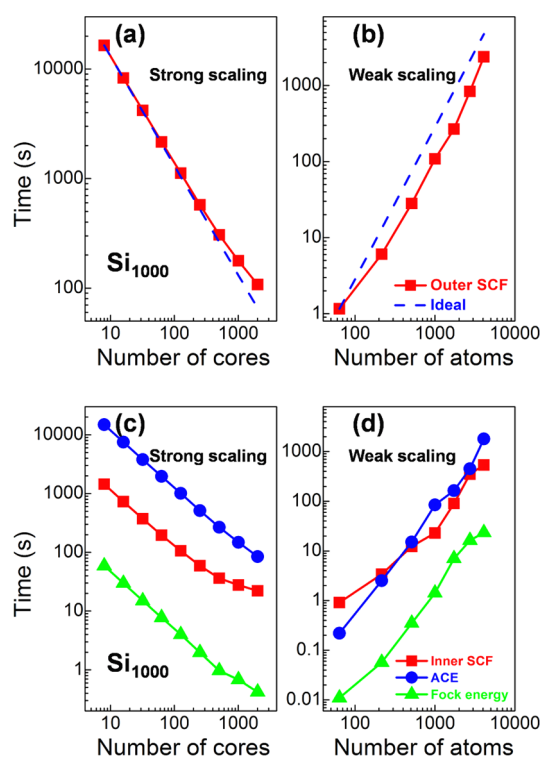
Figure 6. (a) Change of wall clock time in one SCF iteration with respect to the number of cores for the Si_{1000} system (strong scaling). (b) Change of wall clock time with respect to system size on 2000 cores (weak scaling). Panels (c) and (d) show how different components of an ACE-enabled hybrid DFT calculation scale with respect to the number of cores and the system size, respectively.

parallel scalability of the eigensolver used in each inner SCF iteration. Figure 7 shows that the PPCG algorithm exhibits
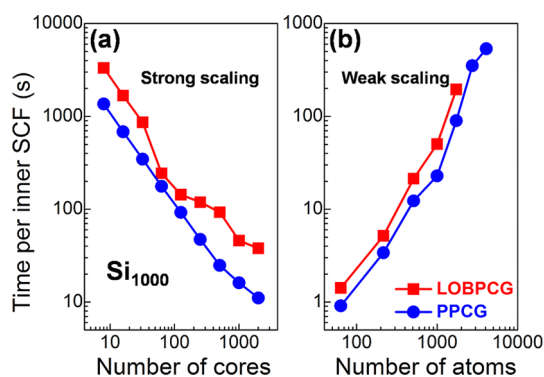
Figure 7. Wall clock time for solving the eigenvalue problems (LOBPCG and PPCG) in one inner SCF iteration with respect to the number of computational cores used for the Si_{1000} system (Strong scaling) and the number of silicon atoms in different systems (Weak scaling). In the case of weak scaling, we use one computational core for each band as the systems increase.

better strong and weak scaling properties than LOBPCG. For the Si_{1000} system (2000 bands), the PPCG-based calculation is roughly 3 times faster than LOBPCG-based calculation. For Si_{1728} (3456 bands), it becomes very expensive to use the LOBPCG algorithm to solve the Kohn−Sham eigenvalue problem because the Rayleigh−Ritz procedure used in the

LOBPCG algorithm requires fully diagonalization of a 10 372 × 10 372 dense matrix.

3.4. Applications to Water Adsorption on Silicene. The reduction in computational cost achieved by ACE and its high parallel scalability enables us to perform hybrid DFT calculations to study the adsorption properties of water molecules on silicene. Because the use of semilocal exchange−correlation functionals are often effective in optimizing the structure of nanosystems[33] and such semilocal DFT calculations are less costly than hybrid DFT calculations, we first use the GGA-PBE[39] exchange−correlation functional with semiempirical long-range dispersion correction proposed by Grimme (DFT-D2)[65] to optimize the nanosystems. The long-range dispersion correction allows us to better describe the weak van der Waals interactions of silicene deposited on substrates and molecular adsorption on the surfaces. We find that DFT-D2 calculations in PWDFT give an accurate bilayer distance of 3.25 Å and a binding energy of −25 meV per carbon atom for bilayer graphene, which fully agrees with previous experimental[66] and theoretical[67] studies. Furthermore, DFT-D2 calculations also give accurate binding energy of −0.26 eV in water molecule dimer.[68] These results confirm the validity of using GGA-based DFT calculations for structural properties. Using a hybrid functional (HSE06) yields similar geometric structures and adsorption properties of water molecules adsorbed on silicene.

It should be noted that semilocal GGA-PBE-based DFT calculations are less reliable in predicting electronic properties (e.g., energy gap) of nanosystems. In particular, PBE-based DFT calculations tend to underestimate the energy gaps of molecules and semiconductors. The use of hybrid DFT calculations often produce more accurate results. For example, GGA-PBE calculations give an energy gap of 6.2 eV for the water molecule, which is smaller than the 8.2 eV returned from a calculation that uses the HSE06 functional in PWDFT. We also cross-checked these calculations against results produced by VASP (Vienna Ab initio Simulation Package) software.[69]

Figure 8 shows the geometric structures of water molecules adsorbed on silicene. Because it is still challenging to obtain freestanding silicene in the experiments, here we consider a silicene sheet deposited on a typical Ag(111) substrate.[70] This system includes 72 silicon (Si) atoms and 256 silver (Ag) atoms denoted by $Si_{72}Ag_{256}$. We study three types of water clusters ($(H_2O)_n$, n = 1, 2, and 3, respectively, for water monomer,
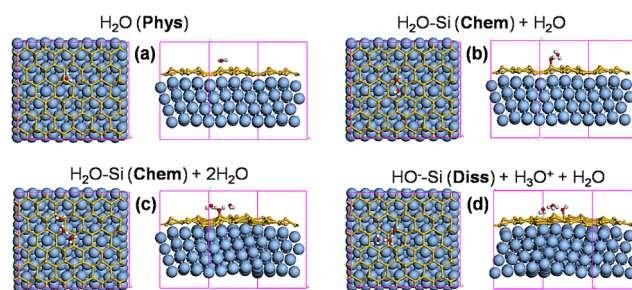
Figure 8. Geometric structures (top and side views) of water molecules adsorbed on silicene supported by the Ag(111) surface, including (a) physisorption of $(H_2O)_1$/silicene/Ag, (b) chemisorption of $(H_2O)_2$/silicene/Ag, (c) chemisorption of $(H_2O)_3$/silicene/Ag, and (d) dissociation of $(H_2O)_3$/silicene/Ag. The yellow, red, white, and blue balls denote silicon, oxygen, hydrogen, and silver atoms, respectively.

dimer, and trimer) adsorption on silicene. We consider two different adsorption configurations for the water trimer on silicene as shown in Figure 8c,d. We adopt the Hartwigsen–Goedecker–Hutter norm-conserving pseudopotentials[63] with valence and semicore states of $1s^1$ for H atom, $2s^2 2p^4$ for O atom, $3s^2 3p^2$ for Si atom, and $4d^{10} 5d^1$ (Including $4d^{10}$ semicore states) for Ag atom in our DFT calculations. The number of occupied states for the $Si_{72}Ag_{256}$ system is 1552. We include 240 unoccupied states in a finite temperature calculation with the temperature set to 300 K. We set the energy cutoff E_{cut} to 40 hartree for these calculations.

The adsorption properties of these optimized systems are listed in Table 4. Our calculations show that water monomer is

Table 4. Adsorption Properties of Water Molecules Adsorption on Silicene, Including Adsorption Type (Phys/Chem/Diss), Adsorption Energy E_a (eV), Adsorption Si–O Bond Length d (Å)

systems	type	E_a	d
(a) $(H_2O)_1$/silicene/Ag	phys	−0.45	2.22
(b) $(H_2O)_2$/silicene/Ag	chem	−1.01	1.90
(c) $(H_2O)_3$/silicene/Ag	chem	−2.29	1.80
(d) $(H_2O)_3$/silicene/Ag	diss	−2.22	1.75

physically adsorbed on Ag-supported silicene (Figure 8a) via weak van der Waals interactions,[30] with small adsorption energy (−0.45 eV) and large adsorption distances (2.22 Å). These properties are similar to those of water monomers adsorbed on graphene.[71] However, the water dimer and trimer molecules adsorbed on Ag-supported silicene show large adsorption energies (−1.01, −2.29, and −2.22 eV) via strong covalent Si–O bonds (1.90, 1.80, and 1.75 Å) between an oxygen atom (O_a) in water and a top silicon atom (Si_a), and thus, they are chemically adsorbed ($H_2O–Si$) on the silicene (Figure 8b,c). Furthermore, this strong adsorption is found to induce dissociation of water trimer on Ag-supported silicene ($HO^-–Si + H_3O^+$) (Figure 8d).

In order to reveal the intrinsic mechanism for such interesting chemical reaction phenomena, we study the electronic structures of water clusters and Ag-supported silicene, which can can help elucidate the interfacial chemical reactions of water molecules adsorption on silicene. Table 5 shows the HOMO, LUMO energies and energy gaps of adsorbate water clusters and work functions of Ag-supported silicene obtained from the GGA-PBE and HSE06 exchange–correlation functional calculations. We find that the GGA-PBE-based DFT calculations yield much lower the energy gaps of

Table 5. Comparison Results of the HOMO Energy E_{HOMO} (eV), LUMO Energy E_{LUMO} (eV), and Energy Gaps E_g (eV) of Adsorbate Water Clusters Computing by the GGA-PBE and HSE06 Exchange–Correlation Functionals[a]

methods	GGA-PBE			HSE06		
systems	E_{HOMO}	E_{LUMO}	E_g	E_{HOMO}	E_{LUMO}	E_g
$(H_2O)_1$ (phys)	−7.2	−1.0	6.2	−8.6	−0.4	8.2
$(H_2O)_2$ (chem)	−6.5	−1.3	5.2	−7.8	−0.9	6.9
$(H_2O)_3$ (chem)	−6.0	−1.2	4.8	−7.4	−0.8	6.6
$(H_2O)_3$ (diss)	−6.2	−1.3	4.9	−7.6	−0.9	6.7

[a]The work functions W_f (eV) of Ag-supported silicene are 4.0 and 4.1 eV, respectively, for the GGA-PBE and HSE06 calculations.

the water clusters (6.2, 5.2, 4.8, and 4.9 eV) compared to that (8.2, 6.9, 6.6, and 6.7 eV) produced by HSE06-based hybrid DFT calculations, although the use of different exchange–correlation functionals results in little effect on the work functions W_f (4.0 and 4.1 eV respectively for the GGA-PBE and HSE06 calculations) of metallic Ag-supported silicene.[33] In the HSE06 calculations, the Fermi level of Ag-supported silicene is closer to the LUMO energies of water clusters than the HOMO energies, indicating the water LUMO should be the reaction orbitals hybridized with the silicon Si $3p_z$ orbitals when water molecules adsorption on silicene. However, the GGA-PBE calculations predict the opposite result that the Fermi level of Ag-supported silicene is closer to the HOMO energies of the water dimer and trimer than the corresponding LUMO energies. Therefore, semilocal GGA-PBE calculations cannot accurately describe the energy positions of HOMO and LUMO of water clusters as well as their energy gaps, and hybrid density functional calculations can significant improve the fidelity of predicting interfacial chemical reactions of molecules adsorption on the substrates.

Figure 9 shows the total density of states (TDOS) of water clusters and Ag-supported silicene computed with the HSE06
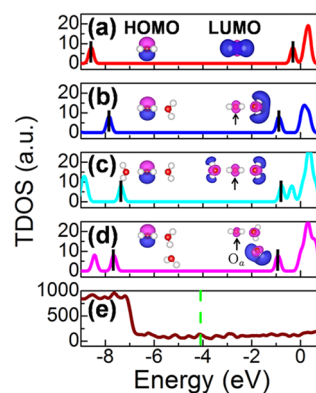
Figure 9. Total density of states (TDOS) of water clusters ((a) $(H_2O)_1$(phys), (b) $(H_2O)_2$(chem), (c) $(H_2O)_3$(chem) and (d) $(H_2O)_3$(diss)) and Ag-supported silicene ((e) silicene/Ag) computed with the HSE06 exchange–correlation functional. The HOMO and LUMO energy levels of water clusters are marked by black solid lines. The HOMO and LUMO states of water clusters are shown in the inset, and the pink and blue regions indicate the positive and negative phase of isosurfaces (0.06 au). The Fermi level of Ag-supported silicene is marked by green dotted lines. All the energy levels are referenced to the vacuum level, which is set to zero. The adsorption oxygen atoms (O_a) of water molecules at the top of silicene are marked by solid black arrows.

exchange–correlation functional. We find that for water monomer, the HOMO and LUMO energies are far away (4.5 and 3.7 eV) from the Fermi level of Ag-supported silicene. Thus, water monomer has a low chemical reactivity to silicene.[32] Due to the interactions between hydrogen-bond acceptor and donor molecules in water dimer and trimer, the LUMO energies get lower (about 3.2 eV) and become closer to the Fermi level as more hydrogen bonds are formed in water clusters. Furthermore, the LUMO states in water dimer and trimer, especially for the adsorption oxygen atoms (O_a) at the top silicon (Si_a) of silicene, are quenched due to the repulsive interactions with neighboring hydrogen-bond molecules, while the HOMO states are almost unchanged in water clusters.[72] Therefore, the LUMO states get more reactive as more

hydrogen bonds are formed in water clusters, which makes the electrons transfer from the Si $3p_z$ orbitals (delocalized broadening is about 4 eV) of Si_a atom in silicene to the O 2s and O $2p_z$ orbitals of O_a atom in water more easier. This effect induces the activated O_a atom to form a Si−O bond upon adsorption, showing an autocatalytic behavior for chemisorption and dissociation compared to water monomer physisorption on silicene. Note that in both Figure 8c,d, the O atom from the H-bond donor water molecule binds with the Si atom in silicene, while the positions of the H-bond acceptors are different. Proton transfer can only occur along the H-bond chain as shown in Figure 8d, resulting in the dissociation of water molecule. On the other hand, such H-bond chain is destroyed into two separated H-bonds as in Figure 8c and thus proton transfer cannot occur. The difference between chemisorption and dissociation is thus caused by the relative position of the H-bond donor and the H-bond acceptors, while the energy difference between the two configurations is small. This is also confirmed from the results in Table 5.

4. CONCLUSIONS

We have described a massively parallel implementation of the recently developed adaptively compressed exchange (ACE) operator formulation for accurate and efficient computation of the exact Hartree−Fock exchange. We compared two iterative algorithms (LOBPCG and PPCG) for solving the Kohn−Sham density functional theory (KSDFT) eigenvalue problems for large-scale hybrid density functional calculations in the plane wave basis set, and we found that PPCG can take advantage of modern high-performance computing architectures more efficiently for systems of large sizes. We demonstrated the efficiency and scalability of our method using hybrid density functional calculations on bulk silicon systems containing up to 4096 atoms. Furthermore, we studied the adsorption properties of water molecules on Ag-supported two-dimensional silicene by using large-scale hybrid density functionals calculations, and we found that water monomer, dimer, and trimer configurations show contrasting adsorption behaviors on silicene. The additional water molecules in dimer and trimer configurations induce a transition from physisorption to chemisorption, followed by dissociation on silicene. Such a hydrogen bond autocatalytic effect is expected to have broad applications in efficient catalysis for oxygen reduction and water dissociation reactions.

AUTHOR INFORMATION

Corresponding Authors
*E-mail: whu@lbl.gov.
*E-mail: linlin@math.berkeley.edu.
*E-mail: asb@lbl.gov.
*E-mail: evecharynski@lbl.gov.
*E-mail: cyang@lbl.gov.

ORCID
Wei Hu: 0000-0001-9629-2121
Lin Lin: 0000-0001-6860-9566

Notes
The authors declare no competing financial interest.

REFERENCES

(1) Verdaguer, A.; Sacha, G. M.; Bluhm, H.; Salmeron, M. *Chem. Rev.* **2006**, *106*, 1478−1510.
(2) Michaelides, A.; Hu, P. *J. Am. Chem. Soc.* **2001**, *123*, 4235−4242.
(3) Ogasawara, H.; Brena, B.; Nordlund, D.; Nyberg, M.; Pelmenschikov, A.; Pettersson, L. G. M.; Nilsson, A. *Phys. Rev. Lett.* **2002**, *89*, 276102.
(4) Michaelides, A.; Ranea, V. A.; de Andres, P. L.; King, D. A. *Phys. Rev. Lett.* **2003**, *90*, 216102.
(5) Brookes, I. M.; Muryn, C. A.; Thornton, G. *Phys. Rev. Lett.* **2001**, *87*, 266103.
(6) Schaub, R.; Thostrup, P.; Lopez, N.; Lægsgaard, E.; Stensgaard, I.; Nørskov, J. K.; Besenbacher, F. *Phys. Rev. Lett.* **2001**, *87*, 266104.
(7) Onda, K.; Li, B.; Zhao, J.; Jordan, K. D.; Yang, J.; Petek, H. *Science* **2005**, *308*, 1154−1158.
(8) Novoselov, K. S.; Jiang, D.; Schedin, F.; Booth, T. J.; Khotkevich, V. V.; Morozov, S. V.; Geim, A. K. *Proc. Natl. Acad. Sci. U. S. A.* **2005**, *102*, 10451−10453.
(9) Wang, Q. H.; Kalantar-Zadeh, K.; Kis, A.; Coleman, J. N.; Strano, M. S. *Nat. Nanotechnol.* **2012**, *7*, 699.
(10) Xu, M.; Liang, T.; Shi, M.; Chen, H. *Chem. Rev.* **2013**, *113*, 3766.
(11) Novoselov, K. S.; Geim, A. K.; Morozov, S. V.; Jiang, D.; Zhang, Y.; Dubonos, S. V.; Grigorieva, I. V.; Firsov, A. A. *Science* **2004**, *306*, 666−669.
(12) Geim, A. K.; Novoselov, K. S. *Nat. Mater.* **2007**, *6*, 183−191.
(13) Castro Neto, A. H.; Guinea, F.; Peres, N. M. R.; Novoselov, K. S.; Geim, A. K. *Rev. Mod. Phys.* **2009**, *81*, 109.
(14) Bianco, E.; Butler, S.; Jiang, S.; Restrepo, O. D.; Windl, W.; Goldberger, J. E. *ACS Nano* **2013**, *7*, 4414−4421.
(15) Li, L.; Lu, S.-Z.; Pan, J.; Qin, Z.; Wang, Y.-Q.; Wang, Y.; Cao, C.-Y.; Du, S.; Gao, H.-J. *Adv. Mater.* **2014**, *26*, 4820−4824.
(16) Dávila, M. E.; Xian, L.; Cahangirov, S.; Rubio, A.; Le Lay, G. *New J. Phys.* **2014**, *16*, 095002.
(17) Li, L.; Yu, Y.; Ye, G.; Ge, Q.; Ou, X.; Wu, H.; Feng, D.; Chen, X.; Zhang, Y. *Nat. Nanotechnol.* **2014**, *9*, 372−377.
(18) Liu, H.; Neal, A. T.; Zhu, Z.; Luo, Z.; Xu, X.; Tománek, D.; Ye, P. D. *ACS Nano* **2014**, *8*, 4033−4041.
(19) Qiao, J.; Kong, X.; Hu, Z.-X.; Yang, F.; Ji, W. *Nat. Commun.* **2014**, *5*, 4475.
(20) Mak, K. F.; Lee, C.; Hone, J.; Shan, J.; Heinz, T. F. *Phys. Rev. Lett.* **2010**, *105*, 136805.
(21) Radisavljevic, B.; Radenovic, A.; Brivio, J.; Giacometti, V.; Kis, A. *Nat. Nanotechnol.* **2011**, *6*, 147−150.
(22) Yin, Z.; Li, H.; Li, H.; Jiang, L.; Shi, Y.; Sun, Y.; Lu, G.; Zhang, Q.; Chen, X.; Zhang, H. *ACS Nano* **2012**, *6*, 74−80.
(23) Qu, L.; Liu, Y.; Baek, J.-B.; Dai, L. *ACS Nano* **2010**, *4*, 1321−1326.
(24) Kostov, M. K.; Santiso, E. E.; George, A. M.; Gubbins, K. E.; Nardelli, M. B. *Phys. Rev. Lett.* **2005**, *95*, 136105.
(25) Guzmán-Verri, G. G.; Lew Yan Voon, L. C. *Phys. Rev. B: Condens. Matter Mater. Phys.* **2007**, *76*, 075131.

(26) Cahangirov, S.; Topsakal, M.; Aktürk, E.; Şahin, H.; Ciraci, S. *Phys. Rev. Lett.* **2009**, *102*, 236804.

(27) Lalmi, B.; Oughaddou, H.; Enriquez, H.; Kara, A.; Vizzini, S.; Ealet, B.; Aufray, B. *Appl. Phys. Lett.* **2010**, *97*, 223109.

(28) Ornes, S. *Proc. Natl. Acad. Sci. U. S. A.* **2014**, *111*, 10899−10899.

(29) Özçelik, V. O.; Ciraci, S. *J. Phys. Chem. C* **2013**, *117*, 26305−26315.

(30) Hu, W.; Wu, X.; Li, Z.; Yang, J. *Phys. Chem. Chem. Phys.* **2013**, *15*, 5753−5757.

(31) Hu, W.; Wu, X.; Li, Z.; Yang, J. *Nanoscale* **2013**, *5*, 9062−9066.

(32) Hu, W.; Xia, N.; Wu, X.; Li, Z.; Yang, J. *Phys. Chem. Chem. Phys.* **2014**, *16*, 6957−6962.

(33) Stroppa, A.; Kresse, G. *New J. Phys.* **2008**, *10*, 063020.

(34) Schimka, L.; Harl, J.; Stroppa, A.; Grüneis, A.; Marsman, M.; Mittendorfer, F.; Kresse, G. *Nat. Mater.* **2010**, *9*, 741−744.

(35) Sun, H.; Mowbray, D. J.; Migani, A.; Zhao, J.; Petek, H.; Rubio, A. *ACS Catal.* **2015**, *5*, 4242−4254.

(36) Hohenberg, P.; Kohn, W. *Phys. Rev.* **1964**, *136*, B864.

(37) Kohn, W.; Sham, L. J. *Phys. Rev.* **1965**, *140*, A1133.

(38) Goedecker, S.; Teter, M.; Hutter, J. *Phys. Rev. B: Condens. Matter Mater. Phys.* **1996**, *54*, 1703.

(39) Perdew, J. P.; Burke, K.; Ernzerhof, M. *Phys. Rev. Lett.* **1996**, *77*, 3865.

(40) Becke, A. D. *J. Chem. Phys.* **1993**, *98*, 1372.

(41) Perdew, J. P.; Ernzerhof, M.; Burke, K. *J. Chem. Phys.* **1996**, *105*, 9982.

(42) Heyd, J.; Scuseria, G. E.; Ernzerhof, M. *J. Chem. Phys.* **2003**, *118*, 8207.

(43) Goedecker, S. *Rev. Mod. Phys.* **1999**, *71*, 1085.

(44) Bowler, D. R.; Miyazaki, T. *Rep. Prog. Phys.* **2012**, *75*, 036503.

(45) DiStasio, R. A., Jr.; Santra, B.; Li, Z.; Wu, X.; Car, R. *J. Chem. Phys.* **2014**, *141*, 084502.

(46) Dawson, W.; Gygi, F. *J. Chem. Theory Comput.* **2015**, *11*, 4655−4663.

(47) Damle, A.; Lin, L.; Ying, L. *J. Chem. Theory Comput.* **2015**, *11*, 1463−1469.

(48) Lin, L. *J. Chem. Theory Comput.* **2016**, *12*, 2242−2249.

(49) Bylaska, E. J.; Tsemekhman, K.; Baden, S. B.; Weare, J. H.; Jonsson, H. *J. Comput. Chem.* **2011**, *32*, 54−69.

(50) Gygi, F.; Duchemin, I. *J. Chem. Theory Comput.* **2013**, *9*, 582−587.

(51) Vecharynski, E.; Yang, C.; Pask, J. E. *J. Comput. Phys.* **2015**, *290*, 73−89.

(52) Knyazev, A. V. *SIAM J. Sci. Comput.* **2001**, *23*, 517−541.

(53) Heyd, J.; Scuseria, G. E.; Ernzerhof, M. *J. Chem. Phys.* **2006**, *124*, 219906.

(54) Giannozzi, P.; Baroni, S.; Bonini, N.; Calandra, M.; Car, R.; Cavazzoni, C.; Ceresoli, D.; Chiarotti, G. L.; Cococcioni, M.; Dabo, I.; Dal Corso, A.; de Gironcoli, S.; Fabris, S.; Fratesi, G.; Gebauer, R.; Gerstmann, U.; Gougoussis, C.; Kokalj, A.; Lazzeri, M.; Martin-Samos, L.; Marzari, N.; Mauri, F.; Mazzarello, R.; Paolini, S.; Pasquarello, A.; Paulatto, L.; Sbraccia, C.; Scandolo, S.; Sclauzero, G.; Seitsonen, A. P.; Smogunov, A.; Umari, P.; Wentzcovitch, R. M. *J. Phys.: Condens. Matter* **2009**, *21*, 395502.

(55) Duchemin, I.; Gygi, F. *Comput. Phys. Commun.* **2010**, *181*, 855−860.

(56) Manzer, S.; Horn, P. R.; Mardirossian, N.; Head-Gordon, M. *J. Chem. Phys.* **2015**, *143*, 024113.

(57) Boffi, N. M.; Jain, M.; Natan, A. *J. Chem. Theory Comput.* **2016**, *12*, 3614−3622.

(58) Lin, L.; Xu, Z.; Ying, L. Adaptively compressed polarizability operator for accelerating large scale ab initio phonon calculations. *Multiscale Model. Simul.* **2017**, *15*, 29−55.

(59) Teter, M. P.; Payne, M. C.; Allan, D. C. *Phys. Rev. B: Condens. Matter Mater. Phys.* **1989**, *40*, 12255.

(60) Lin, L.; Lu, J.; Ying, L.; E, W. *J. Comput. Phys.* **2012**, *231*, 2140−2154.

(61) Hu, W.; Lin, L.; Yang, C. *J. Chem. Phys.* **2015**, *143*, 124110.

(62) Hu, W.; Lin, L.; Yang, C. *Phys. Chem. Chem. Phys.* **2015**, *17*, 31397−31404.

(63) Hartwigsen, C.; Goedecker, S.; Hutter, J. *Phys. Rev. B: Condens. Matter Mater. Phys.* **1998**, *58*, 3641.

(64) Auckenthaler, T.; Blum, V.; Bungartz, H. J.; Huckle, T.; Johanni, R.; Krämer, L.; Lang, B.; Lederer, H.; Willems, P. R. *Parallel Comput.* **2011**, *37*, 783−794.

(65) Grimme, S. *J. Comput. Chem.* **2006**, *27*, 1787−1799.

(66) Zacharia, R.; Ulbricht, H.; Hertel, T. *Phys. Rev. B: Condens. Matter Mater. Phys.* **2004**, *69*, 155406.

(67) Hu, W.; Li, Z.; Yang, J. *J. Chem. Phys.* **2013**, *138*, 054701.

(68) Carter, D. J.; Rohl, A. L. *J. Chem. Theory Comput.* **2012**, *8*, 281−289.

(69) Kresse, G.; Hafner, J. *Phys. Rev. B: Condens. Matter Mater. Phys.* **1993**, *47*, 558.

(70) Feng, B.; Ding, Z.; Meng, S.; Yao, Y.; He, X.; Cheng, P.; Chen, L.; Wu, K. *Nano Lett.* **2012**, *12*, 3507−511.

(71) Leenaerts, O.; Partoens, B.; Peeters, F. M. *Phys. Rev. B: Condens. Matter Mater. Phys.* **2008**, *77*, 125416.

(72) Hermann, A.; Schmidt, W. G.; Schwerdtfeger, P. *Phys. Rev. Lett.* **2008**, *100*, 207403.